Abstract

This report outlines two distinct projects undertaken for the TRINAT experiment at TRIUMF. The first was the investigation of the ability to turn off a magnetic field used to create a Zeeman shift in atomic energy levels. A detailed account of the properties of the field is provided, including a thorough investigation of eddy current effects. It was found that the field could be turned off in $410\,\mu s$ or less, depending on the experimental setup. The second part of the report is a discussion of locking a laser diode to particular frequency using saturation spectroscopy in ^{39}K and setting up a system for optical pumping of ^{41}K. This includes an outline of the process of putting RF sidebands on the laser.

Contents

List of Figures

List of Tables

1 Magnetic Field

1.1 Introduction

The TRINAT (**TRI**UMF **N**eutral **A**tom **T**rap) project at TRIUMF studies the $\beta - \nu$ correlation in radioactive β decay. This provides a low energy test of the Standard Model and constitutes a search for non-Standard Model scalar bosons. In order to accurately reconstruct the neutrino momentum, it is necessary to have a localized source of atoms suspended in space [1]. To achieve this, a magneto-optical trap (MOT) is used. The purpose of the magnetic field is to create a Zeeman shift in the atomic energy levels. The Zeeman shift increases the probability of absorbing circularly polarized light and thus is necessary in trapping atoms. Furthermore, it is necessary to have this magnetic field turned off (effectively turning off the trap) in order to polarize the trapped atoms by way of optical pumping. Ideally, we would like to achieve a duty cycle of $1\,ms$ on, $1\,ms$ off. Thus, we were interested in how quickly we could turn off the field, how uniformly the field decreased, whether induced fields affected the fall time, etc. To begin, it will be necessary to discuss how the magnetic field was generated and some basic properties of a MOT.

1.2 MOT Basics

Consider a collection of atoms between two counter-propagating laser beams, each tuned slightly below resonance. If the atoms are moving in one direction, they will see one laser blue shifted and the scattering rate from that laser will increase, see Figure 1. This results in a net acceleration in the direction of propagation of that laser beam. The same process is true for an atom moving in the opposite direction. This is effectively a damped harmonic oscillator. This effect slows atoms down until their average velocity is zero (with temperatures $< 1\,mK$). This is known as optical molasses.

Now add a magnetic field and make the light circularly polarized, see Figure 2. The atoms will have their energy levels Zeeman shifted due to the external magnetic field [2]. Now the probability of absorbing right circularly polarized light is enhanced in one direction and the probability of absorbing left-circularly polarized light is enhanced in the other. This effect drives the atoms to the zero point of the magnetic field. One achieves a collection of

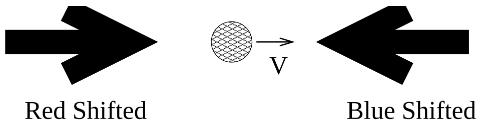

Figure 1: Two counter-propagating laser beams incident on a collection of atoms. Due to the motion of the atoms, one laser appears blue shifted while the other appears red shifted.

cooled, trapped atoms. This is known as a magneto-optical trap.

1.3 Properties of the Magnetic Field

To create the magnetic field, two parallel coils of wire were used. Current was run through them in opposite directions creating a quadrupole field. This configuration is sometimes referred to as an anti-Helmholtz configuration (see Figure 2), whereas a Helmholtz configuration has the currents running in the same direction. This terminology will be adopted for the rest of the paper.

For a quick analysis of these fields we can proceed using the Biot-Savart law (this is only applicable along the centre axis of the two coils). The magnetic field, $\mathbf{B}$, at a distance r from a current element $I\,d\mathbf{z}$ is given by, [3]

$$d\mathbf{B}(z) = \frac{\mu_o}{4\pi}\frac{I\,d\mathbf{z}\times\hat{r}}{r^2} \tag{1}$$

Applying this to the geometry shown in Figure 3 with N turns of wire we obtain,

$$\mathbf{B}(z) = \frac{NI\mu_o}{2}\left\{\frac{\frac{s}{2}-z}{((\frac{s}{2}-z)^2+R^2)^{\frac{1}{2}}} - \frac{\frac{s}{2}-z-t}{((\frac{s}{2}-z-t)^2+R^2)^{\frac{1}{2}}} + \frac{\frac{s}{2}+z}{((\frac{s}{2}+z)^2+R^2)^{\frac{1}{2}}} - \frac{\frac{s}{2}+z-t}{((\frac{s}{2}+z-t)^2+R^2)^{\frac{1}{2}}}\right\} \tag{2}$$

This is nothing more than a direct application of the Biot-Savart law integrated over a finite thickness of wire. A nice check of this equation is to let $t = \frac{s}{2}$, this implies the two coils are so thick that they “meet”. This indeed happens mathematically and we obtain the magnetic field of a solenoid of length s (see for example problem 5.2 (a), pg. 205 of reference [4]). A plot

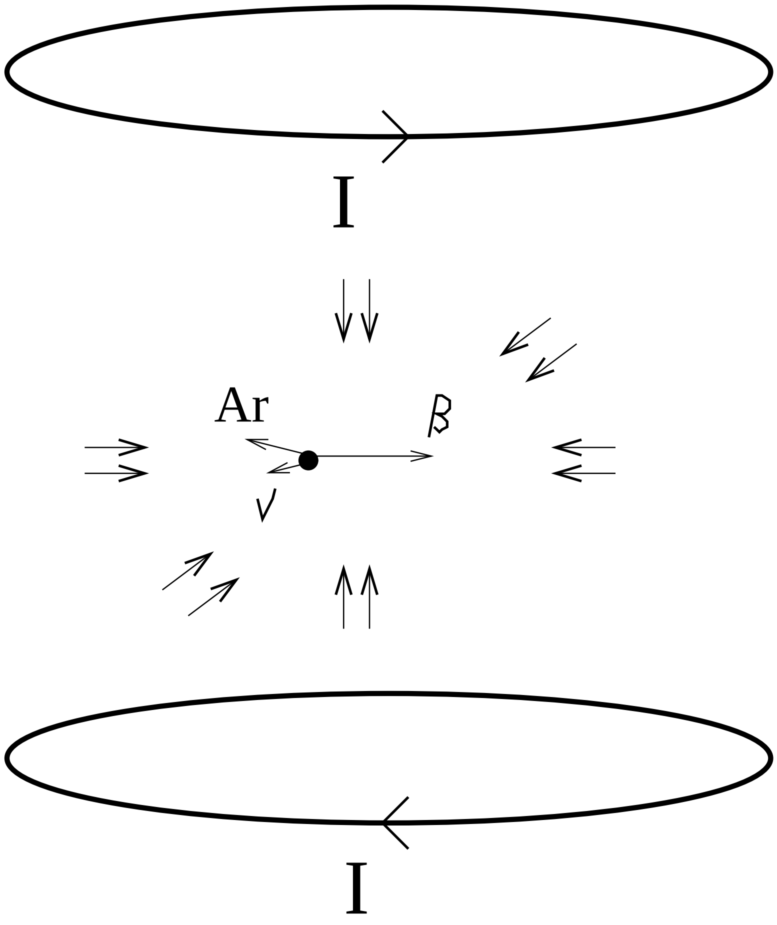

Figure 2: Anti-Helmholtz coils within a MOT. The arrows represent counter-propagating beams of circularly polarized light in three dimensions. The products of β decay are shown at the centre.

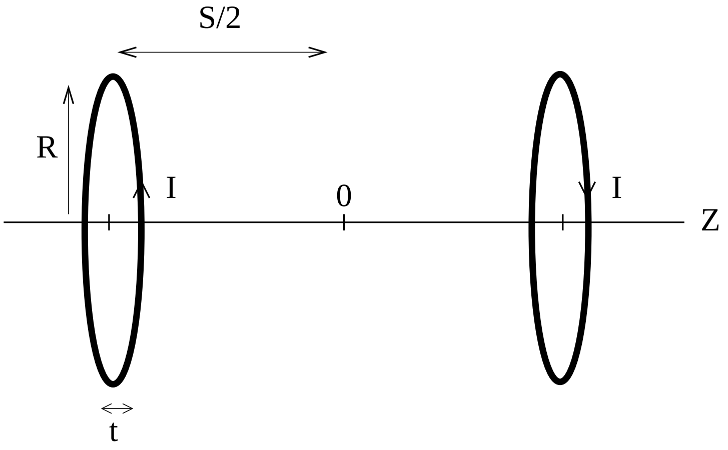

Figure 3: Geometry for anti-Helmholtz coils. Coils now have a thickness, t, and are separated by a distance s.

of equation (2) with thin coils is shown in Figure 4 for both Helmholtz and anti-Helmholtz configurations. In both cases the field is at a maximum at the centre of either coil and a local minimum at the midpoint between the two coils. It was found that the presence of a coil thickness less than $\sim 20\%$ of the distance between the coils had a very small effect on the field, that is, the field looked essentially as it would for thin coils. In our setup this roughly holds true; the coil thickness ranges from approximately $2 \rightarrow 5\,cm$ (depending on the coils used), while the separation ranges from approximately $15 \rightarrow 20\,cm$.

If we wish to investigate the field off the centre axis, we need to resort to approximate expressions. These are given on page 179 of reference [4]. Upon calculating the first few terms it was found that the field changed at the rate of about $0.5\%/mm$ near the centre of the two coils. Changes of this magnitude were small enough to ignore for our purposes since we were only interested in the region near the centre of the coils, approximately within $5\,mm$.

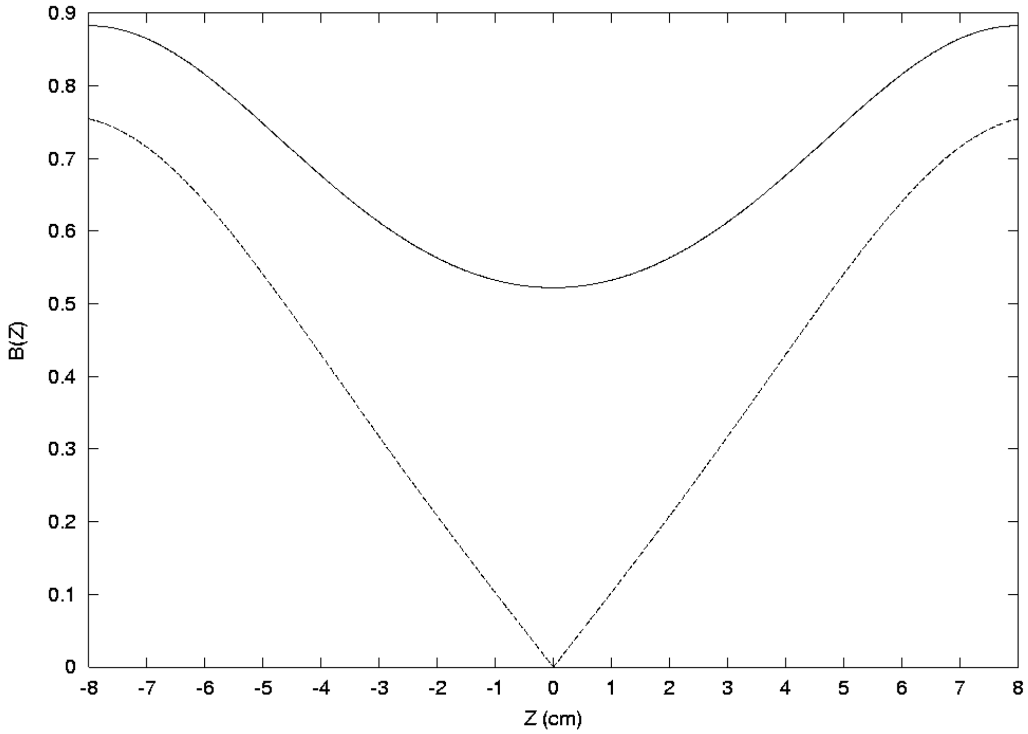

Figure 4: Anti-Helmholtz and Helmholtz fields along the centre axis. The anti-Helmholtz field goes to zero at the midpoint between the two coils. A coil separation of $16.4\,cm$, coil radius of $7.65\,cm$, and coil thickness of $1\,cm$ were used. $B(z)$ is arbitrary units, however, we typically dealt with fields from $10 \rightarrow 50\,G$ depending on the current.

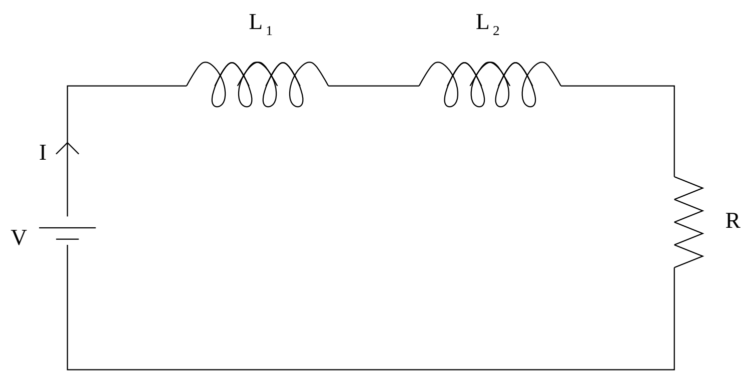

Figure 5: Coil circuit.

1.4 Inductance

Now that we have an idea of how the magnetic field is set up we would like to gain some insight into how it behaves when we turn it on and off. The power to the coils was provided by a Russian Coil Driver which quickly turns on using the combination of a high voltage "boost" pulse ($48\,V$) and a low voltage ($5\,V$) steady supply [5]. As the boost pulse decays the low voltage steadily increases; the overall effect is a rapid turn on ($\leq 200\,\mu s$) to a constant voltage. The length of time the boost pulse is on can be adjusted in conjunction with the low voltage supply to obtain a constant current and thus constant magnetic field. The driver was designed for a duty cycle of $2.5\,ms$ on, $2.5\,ms$ off. It may not be capable of driving a $1\,ms$ on, $1\,ms$ off cycle as the power transistors may overheat.

It is useful to know how quickly the field turns on, however, we were far more interested in how quickly it turned off. For these purposes it is necessary to investigate the nature of the circuit more thoroughly.

Consider the circuit shown in Figure 5. Applying the loop rule in the direction of current we obtain,

$$V - L_1\frac{dI}{dt} - L_2\frac{dI}{dt} + 2M\frac{dI}{dt} - RI = 0 \tag{3}$$

where L_1 and L_2 are the inductances of the coils and M is the mutual inductance of the coils.

This has the solution,

$$I(t) = \frac{V}{R}(1 - e^{-\frac{t}{\tau}}) \tag{4}$$

where

$$\tau = \frac{L_1 + L_2 - 2M}{R} \tag{5}$$

Immediately, we can see that if we drive each coil separately (effectively setting either L_1 or L_2 to zero in our analysis) we can speed up the fall time.

In addition, we can estimate the size of the mutual inductance by running the coils in the Helmholtz and anti-Helmholtz configurations and comparing the fall times. The reason is that τ for the Helmholtz case is given by,

$$\tau = \frac{L_1 + L_2 + 2M}{R} \tag{6}$$

so the difference between the τ's is proportional to the mutual inductance.

1.5 Eddy Currents

In the presence of a non-zero $\frac{dB}{dt}$, currents will be induced in any nearby conducting materials. This is encapsulated in Faraday's law,

$$\nabla \times \mathbf{E} = -\frac{\partial \mathbf{B}}{\partial t} \tag{7}$$

which states that an electric field is induced by a changing magnetic field.

This is the basis behind eddy currents. An eddy current is the general name given to an induced current loop in a conducting material due to a changing magnetic field.

We can model eddy current effects by assuming many small closed current loops are induced in conducting materials subject to a finite $\frac{dB}{dt}$, see Figure 6. The direction of the induced current is given by Lenz's law, i.e. the field generated by the induced current opposes the change in flux which created it.

In general, the presence of eddy currents will tend to increase the fall time, i.e. they will cause the field to take longer to shut off. However, in the

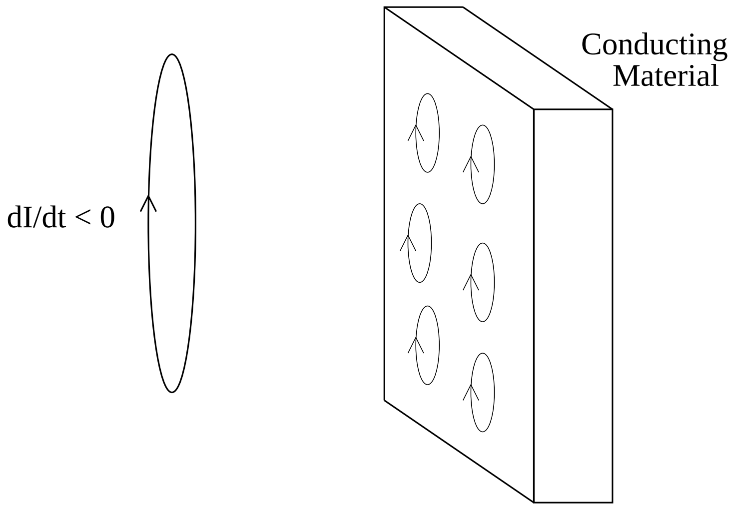

Figure 6: Simple picture of eddy currents. The case of a decrease in current is shown. If current was increasing ($\frac{dI}{dt} > 0$), the induced current loops would be in the opposite direction.

anti-Helmholtz configuration the induced current loops from each coil were in opposite directions (since the currents in the main coils were opposite to each other). Thus, some cancellation should occur. Conversely, in the Helmholtz configuration, the eddy current loops add and make the fall time even longer.

As an example of this, consider a conducting sheet in the centre of the two coils, see Figure 7. The induced currents will completely cancel due to the symmetry with respect to the coils. Therefore, the severity of eddy current effects is dependent on two factors: (i) the amount of conducting material nearby (and its conductivity), and (ii) the location of the conducting materials with respect to the coils. If the eddy current sources are symmetric with respect to the coils some cancellation occurs. In our setup, the largest piece of conducting material nearby was the vacuum chamber which contained the atoms to be trapped and pumped. Fortunately, the coils will be mounted such that the location of metal from the chamber is approximately symmetric to the coils. At this point it will be useful to begin a more quantitative analysis of some of the phenomena discussed.

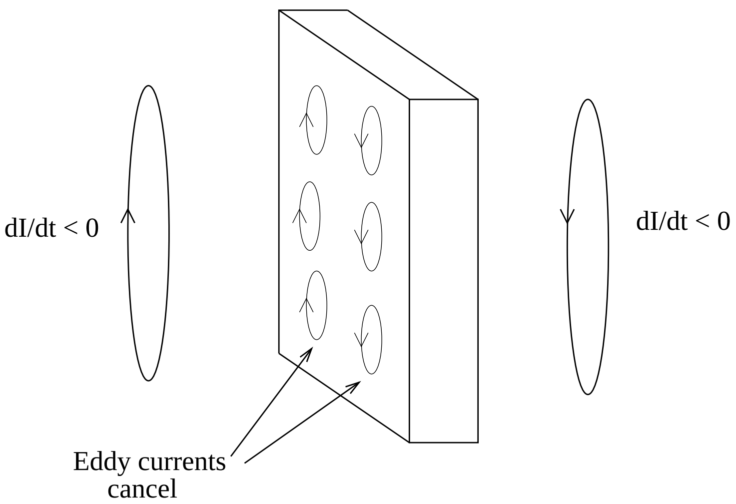

Figure 7: Cancellation of eddy currents. Due to the opposite directions of current in the main coils, the induced currents cancel.

1.6 Magnetic Field Measurements

Initially, measurements of the magnetic field were obtained using a small ($\sim 5\,cm$ diameter) coil of wire. This "pick-up" coil gave a measure of $\frac{dB}{dt}$. The waveforms obtained were integrated to extract the field, B. The rise and fall times could be estimated by looking at either B or $\frac{dB}{dt}$. Later, a $20\,kHz$ Hall Probe was used to directly measure the field. This method was significantly more useful since one could probe the field in real time. Yet another way to measure the field is to measure the current in the main coils. However, this method is not entirely revealing since induced fields may be present that don't significantly affect the current in the main coils.

To get a feel for what was measured, a typical anti-Helmholtz field is shown in Figure 8. This was taken in the absence of any conducting materials with the coils separated by $15\,cm$, the approximate distance they would be separated by if they were mounted on the chamber. The plot shows the field in volts, which is directly proportional to the magnitude of the field in Gauss ($0.1\,V = 10\,G$) and thus adequate for our purposes since we were primarily

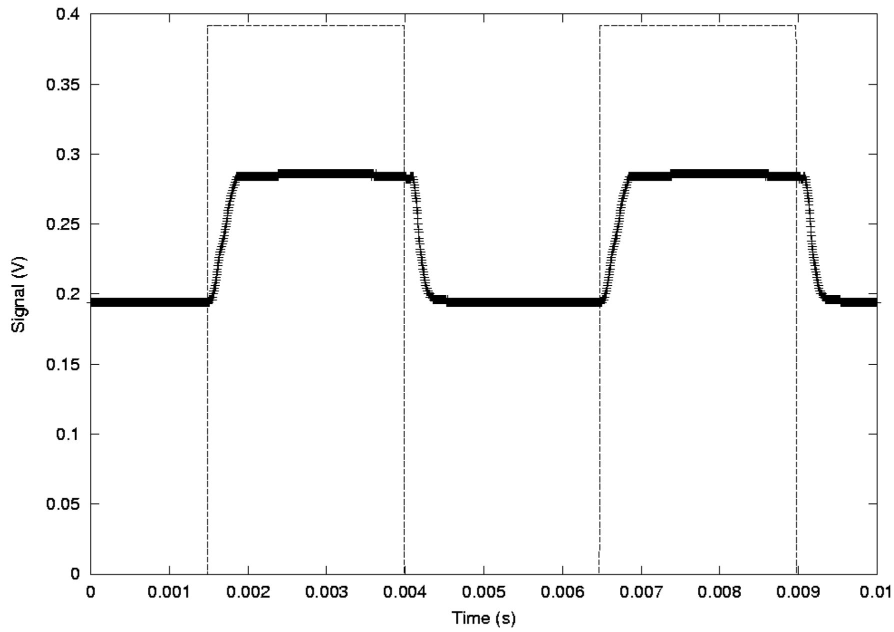

Figure 8: Anti-Helmholtz field measured with a $20\,kHz$ Hall Probe. Signal (in volts) is proportional to the magnitude of the field. The logic signal which triggers the turn on and turn off of the field is also shown.

interested in the fall time.

In Figure 9, plots of the decrease in field are shown for an anti-Helmholtz field with and without conducting material present (also measured with the Hall Probe). Two separate Russian Coil Drivers were used to drive the coils. The current through the coils was approximately $19\,A$. The curve with the longer fall time had two solid aluminum blocks ($\sim 8\,cm$ square) placed at the centre of each coil. The presence of these eddy current sources slowed down the turn off, as expected.

The 95% fall times were computed for each curve in Figure 9. That is, the time from when the field began to decrease until the point at which it had decreased to 95% of its original value. The values were: $77\,\mu s$ for the setup with no eddy current sources and $172\,\mu s$ for the setup with eddy current sources. These values are roughly a lower limit on the fall time

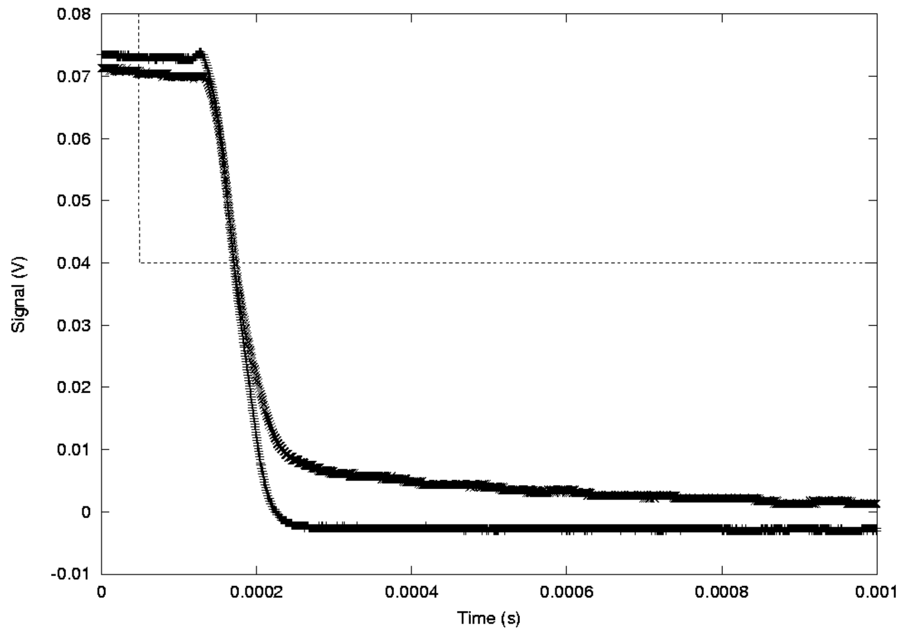

Figure 9: Anti-Helmholtz field with and without eddy current sources. The fall time for the setup with eddy current sources is longer than the one with no eddy current sources.

since the resolution of the data was not fine enough to exactly pinpoint the 95% location. This is also the reason for not using the 99% fall time as an indicator of the field turning off. The resolution was not fine enough to clearly distinguish the 99% fall time with any reasonable degree of accuracy. By comparing numerous fall times with their respective curves it was estimated that these values could be greater by as much as $50\,\mu s$.

In an attempt to check the magnitude of mutual inductance effects, fall times were measured for both the Helmholtz and anti-Helmholtz configurations (without eddy current sources). In addition, one driver was used to check the assumption that using two drivers should decrease the fall time. The results were: $286\,\mu s$ for the Helmholtz setup and $245\,\mu s$ for the anti-Helmholtz setup. Again, an error of approximately $0 \rightarrow 50\,\mu s$ can be attributed to these values. These results support the previous claims: (i) the values are of similar magnitude, indicating mutual inductance effects are small, and (ii) the values are significantly larger than those obtained with two separate drivers, indicating that a less inductive load decays more rapidly.

A measurement of the fall time with the coils mounted on the chamber, with two drivers, in the anti-Helmholtz setup, yielded a 95% fall time of $118\,\mu s$. Once again, an error of approximately $0 \rightarrow 50\,\mu s$ is estimated. The probe was located approximately $2\,cm$ from the centre of the chamber and $29\,A$ was running through each coil. The field is shown in Figure 10 and the explicit decrease is shown in Figure 11.

In addition, measurements were made with bias field coils nearby (i.e. coils that will be run with constant current to extinguish stray magnetic fields, mainly the Earth's). These measurements were taken inside the chamber while the bias coils (one pair) were outside the chamber. Results showed a negligible effect. However, for the main coils in free space, an effect was noticeable when the bias coils were shorted out. This effect was enough to double the fall time in some cases. With the bias coils connected to a DC power supply, the effect was much smaller (approximately 25% longer fall time).

Another useful application of the Hall Probe was in checking the approximate range over which eddy current effects were significant. By placing eddy current sources (aluminum blocks, aluminum pipes, stainless steel gaskets, copper flanges) at various distances and probing the field between the coils (with the coils in free space) it was found that any eddy current source beyond approximately $10\,cm$ had a negligible effect on the fall time. Within $10\,cm$ the effect became more prominent as the source was moved closer. The effect of sources outside the chamber on the field in the chamber was very small.

A number of problems were encountered throughout the course of these measurements. The most persistent of these were "spikes" in the profile of the magnetic field. It was found that depending on the coil setup (Helmholtz or anti-Helmholtz) and the location of the Hall Probe, one could find regions in which the magnetic field had large negative or positive going spikes. These spikes were also observed when an attempt was made to find the zero field position in the anti-Helmholtz setup, see Figure 12. The magnitude of the spikes could be as large as the original field itself, depending on the probe position, etc. In addition, the presence of spikes significantly affected the fall time.

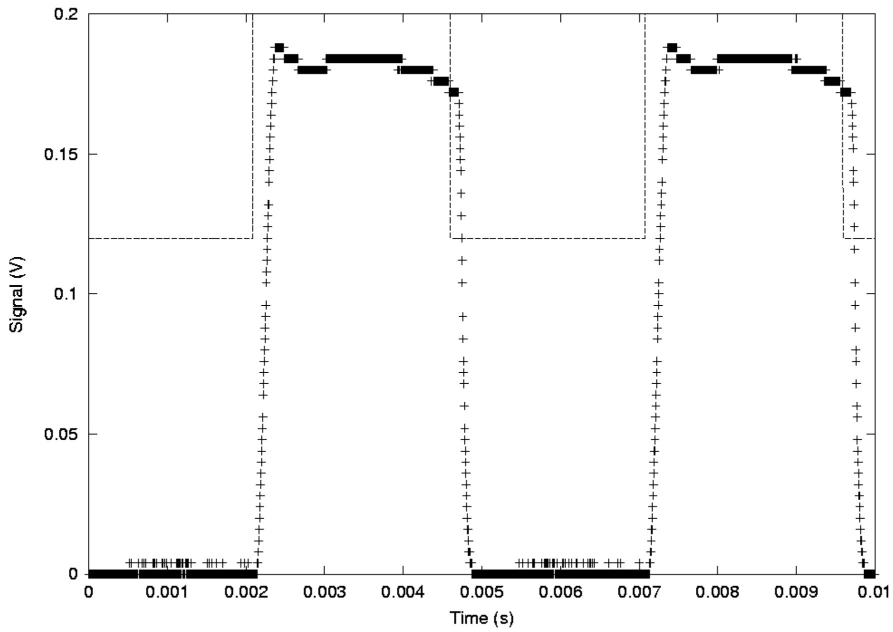

Figure 10: Anti-Helmholtz field inside the chamber. The logic pulse is also shown.

Initially it was thought that the spikes may be the result of a phase difference in the driving frequencies of the coil drivers. That is, one coil may be turning on or off later than the other causing an asymmetric field and possibly causing the spikes. For this reason, the characteristics of each driver were throughly examined. It was found that the drivers were not identical in the magnitude and time duration of the boost pulses and their interplay with the low voltage supply. That is, it may not ever be possible to drive the coils in an identical fashion. This is useful to know, however, it was observed that this effect was not significant enough to generate the spikes. Eventually it was discovered that the shaft of the Hall Probe and power cord attached to it were picking up significant fields. For example, the spikes could be altered in magnitude simply by moving the power cord. This pick-up is almost certainly the origin of the spikes. This doesn't invalidate our previous results of fall times, etc., however, it does cast a greater uncertainty on the

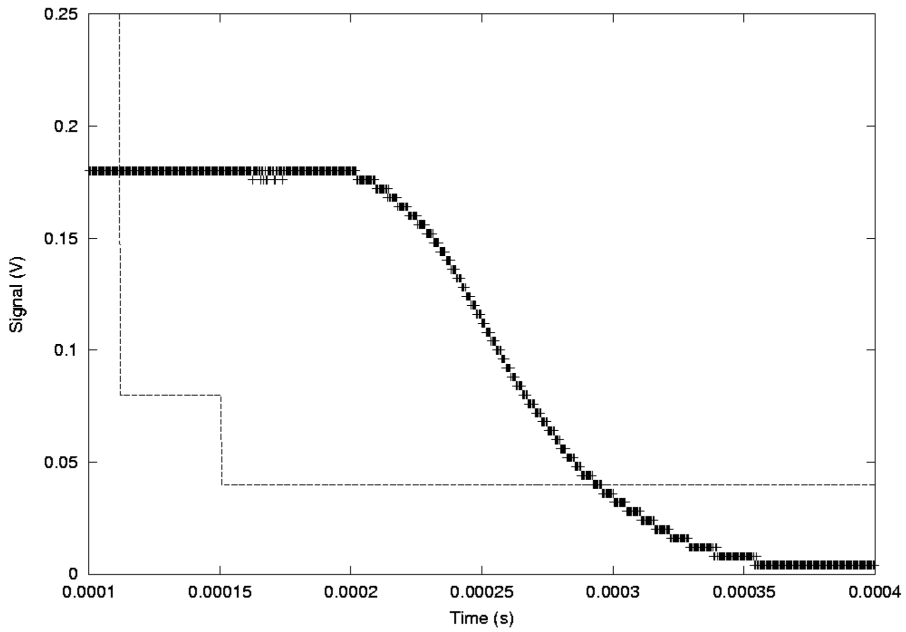

Figure 11: Decrease of the anti-Helmholtz field inside the chamber.

measurements.

Another characteristic of the setup was that after the logic went to zero there was an approximate $100\,\mu s$ delay before the field started decreasing (see Figures 9 and 11 for example). This was observed with both the Hall Probe and the pick-up coil so was most likely an artifact of the driver itself. However, this doesn't present a problem since we were only concerned with how long it takes for the field to decrease from a constant value, it is inconsequential if this is slightly shifted in time.

1.7 Conclusions

Numerous experimental difficulties were encountered in accurately determining the fall time of the magnetic field, these included: resolution of the data, asymmetry of the drivers, unexplained delay of the current turn off time, and especially pick-up noise from the probe. For this reason, only general

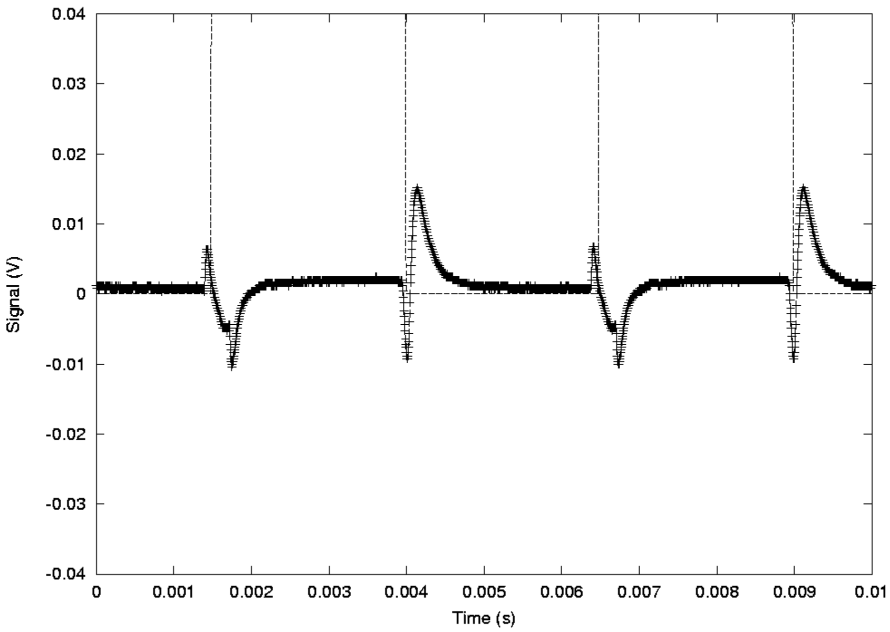

Figure 12: Zero point for anti-Helmholtz field. This was as close to zero as could be found. Notice the presence of artifical spikes in the field due to pick-up from the Hall Probe.

conclusions can be reached. One of these general conclusions is that at no time was a 95% fall time greater than $410\,\mu s$ observed for the magnetic field in the anti-Helmholtz setup with two separate drivers. That is, no matter how large the spikes were, or how many eddy current sources were present, the 95% fall time was always less than $410\,\mu s$, and often much less than this (for example, $118\,\mu s$ for the coils mounted on the chamber).

In summary, it was found that mutual inductance effects were small and eddy current effects were significant depending on position of the sources. There were several artifacts of the probe and drivers that complicated the measurements. And, the fall time of the field for the anti-Helmholtz setup with two drivers lies approximately in the range 100 to $400\,\mu s$.

2 Saturation Spectroscopy and Optical Pumping

2.1 Introduction

In order to optically pump trapped atoms we first needed to lock a diode laser to a resonance of potassium using saturation spectroscopy. This was achieved by irradiating a vapour cell of natural K ($\sim 93\%\ ^{39}K$ and $\sim 7\%\ ^{41}K$ with counter-propagating strong and weak laser beams (the so-called pump and probe laser beams) and observing the absorption versus frequency curve. Further details of this procedure are outlined elsewhere and will be omitted from this paper. Then a lock-in amplifier is used to lock to a particular resonance. Once a peak has been selected as the locking peak, a setup can be implemented to achieve optical pumping.

In order to optically pump atoms, one needs to set the laser frequency to that of the desired atomic transition. The procedure to achieve this once a locking peak is known is as follows: use a voltage controlled oscillator to oscillate the laser diode at a particular frequency (in our case RF), this creates replicas of the atomic absorption peaks at $\nu_{peak} \pm \nu_{RF}$ and allows us to tune the frequency splitting between these peaks. Then, two acousto-optic modulators (AOM's) are used to offset the lock-in frequency to match the exact transition of interest. This procedure should become clear once our particular setup is discussed. As a reference, the complete setup is shown in Figure 13.

2.2 Atomic Energy Levels

Our saturation spectroscopy setup contains stable ^{39}K. We use one of its resonances to lock the laser. We then work from this lock-in frequency to achieve a setup for optical pumping of ^{41}K. To do this, we first need to know something about the atomic transitions of these isotopes.

The ground and first excited state splittings of both ^{39}K and ^{41}K are shown in Figures 14 and 15. Transitions between these levels give rise to the resonance structure of the isotope that we were interested in. The explicit transitions are given in Tables 1 and 2. The transitions which are necessary for optical pumping of ^{41}K are the $F = 1 \rightarrow F = 2$ and the $F = 2 \rightarrow F = 2$ transitions.

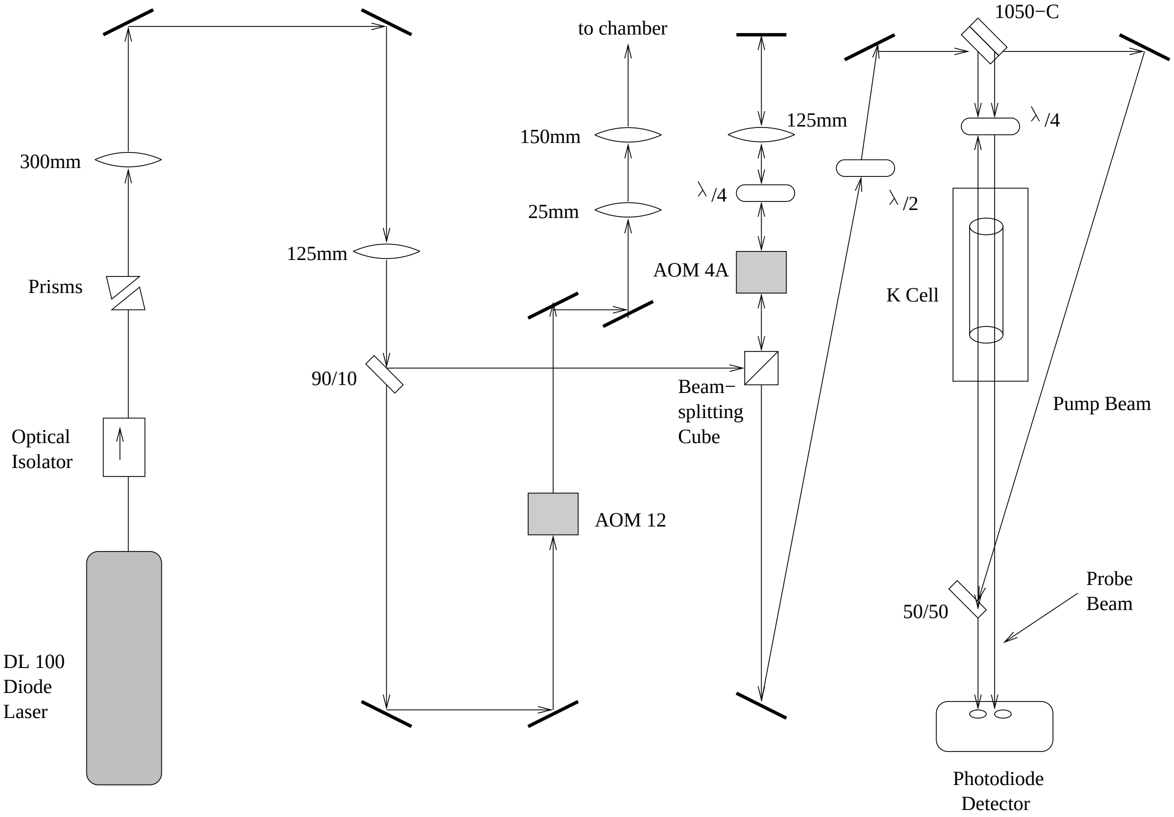

Figure 13: Setup for saturation spectroscopy and optical pumping.

Transition	Frequency (MHz)
$F = 1 \rightarrow F = 1$	254.38
$F = 1 \rightarrow F = 2$	309.38
$F = 2 \rightarrow F = 1$	-207.63
$F = 2 \rightarrow F = 2$	-152.63

Table 1: Atomic transitions for ^{39}K between the ground and first excited state.

Transition	Frequency (MHz)
$F = 1 \rightarrow F = 1$	375.92
$F = 1 \rightarrow F = 2$	406.30**
$F = 2 \rightarrow F = 1$	121.91
$F = 2 \rightarrow F = 2$	152.29**

Table 2: Atomic transitions for ^{41}K between the ground and first excited state.

Transitions can also occur from the midpoints of the splittings of either state, thus giving rise to so-called crossover peaks [6]. The absorption versus frequency curve is shown at the top of Figure 16.

The centre group of peaks arise as part of performing saturation spectroscopy and are not of interest to us. The curve is normalized such that the first peak is at $0\,MHz$. Notice the following peaks are at $27.5\,MHz$ (crossover peak), and $55\,MHz$ (excited state splitting of ^{39}K). Then the next set of peaks are $462\,MHz$ away (ground state splitting ^{39}K).

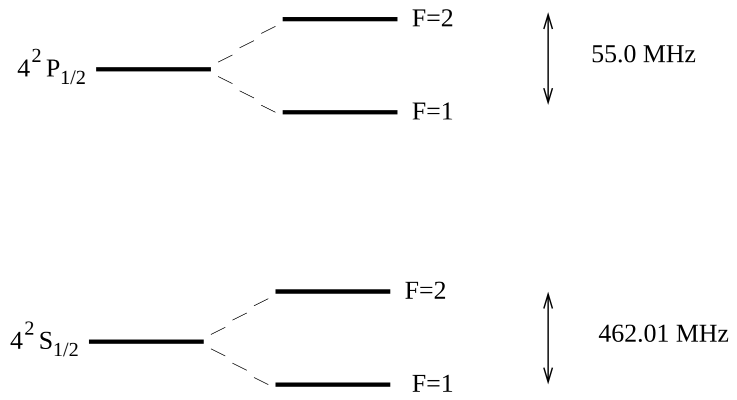

Figure 14: Atomic energy levels for ^{39}K for the ground and first excited state.

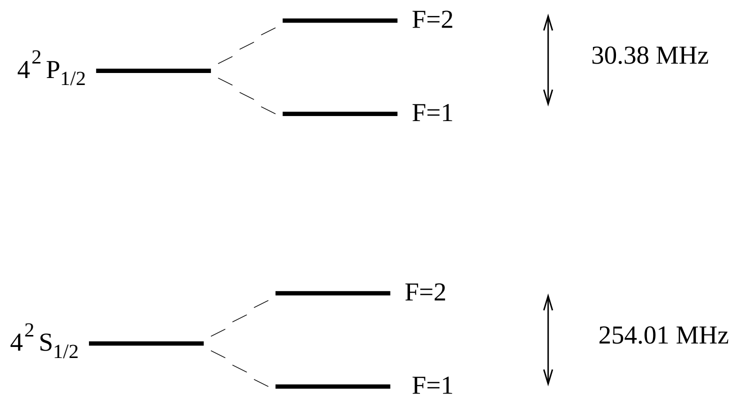

Figure 15: Atomic energy levels for ^{41}K for the ground and first excited state.

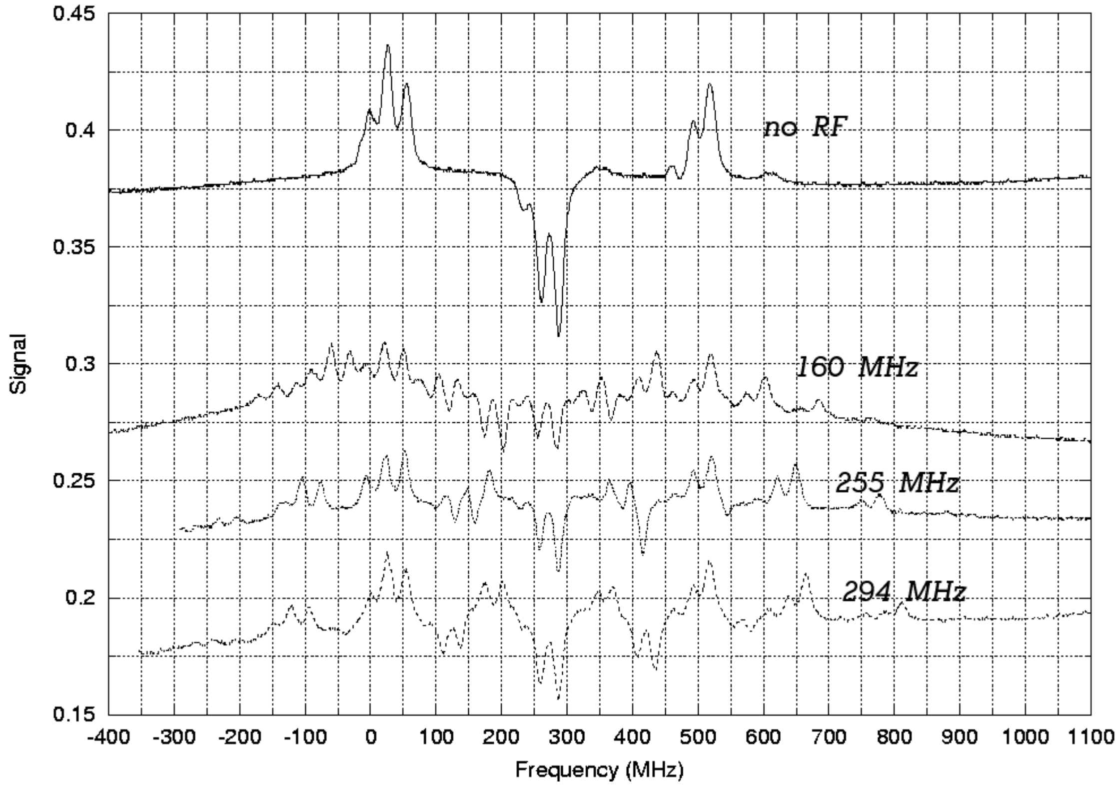

Figure 16: Resonance peaks for ^{39}K with various RF frequencies. The top curve is for no RF oscillations, the next lowest is for an RF of $160\,MHz$, next lowest for $255\,MHz$, and the lowest for $294\,MHz$. Notice the position of the replica peaks correspond to the RF value.

2.3 RF Driver

The RF creates replicas of the peaks at $\nu_{peak} \pm \nu_{RF}$. This is often referred to as putting "sidebands" on the laser [7]. In addition, a form of crossover peaks are created at $\nu_{peak} \pm \frac{\nu_{RF}}{2}$. The reason for applying the RF is to have a method by which we can adjust the frequency splitting of the sidebands to match that of the energy level splitting of interest. In our case, we want $\nu_{RF} = 254.01\,MHz$ to match the ground state splitting of ^{41}K. Figure 16 shows the peak structure for three different RF values with a input voltage of $12\,VDC$ to the driver.

A few technical characteristics of the RF driver, namely power output with rms voltage and laser peak power with RF frequency, are presented in the tables below. The laser peak power measurements were done by putting the light into a $1\,ns$ detector and then taking the FFT with a $100\,MHz$ digital storage scope.

RMS Voltage (V)	Power (dBm)	Power (mW)
2.25	+20	100
0.71	+10	10
0.64	+9	8
0.225	0	1
0.071	-10	0.1

Table 3: RF power with voltage.

2.4 Acousto-Optic Modulators

The next step on our way to achieving optical pumping was implementing two AOM's to offset the frequency. In simple terms, an AOM is a device which shifts the laser frequency by diffracting light off a crystal by oscillating it with a sound wave. For our purposes, it is sufficient to know that an AOM provides a variable shift in the laser frequency. Recall that our goal is to go from our locking system of ^{39}K to an optical pumping system for ^{41}K. The RF driver was used to tune the splitting of the sidebands and now two AOM's will be used to perform a frequency shift. Specifically, we use the

RF Frequency (MHz)	Laser Peak Power (dBm)
126	28.0
146	32.8
166	28.4
186	22.0
206	22.4
226	15.2
246	6.8

Table 4: Laser peak power with RF frequency.

AOM's to shift the frequency such that the sidebands (split by ν_{RF}) match the $F = 1 \to F = 2$ and $F = 2 \to F = 2$ transitions in ^{41}K.

Once the AOM's were properly mounted we were in a position to determine a locking peak and set the AOM's and RF to the appropriate values for optical pumping. First, we decided to lock the laser to the peak corresponding to the positive RF crossover peak of the $F = 1 \to F = 2$ transition in ^{39}K. That is, the peak at a frequency,

$$\nu_{lock} = \nu_{1\to2} + \frac{\nu_{RF}}{2} \tag{8}$$

We know ν_{RF} and $\nu_{1\to2}$, thus,

$$\nu_{lock} = 436.39\, MHz \tag{9}$$

Now, a double pass AOM (ν_{dp}) allows us to offset the laser frequency such that,

$$\nu_{laser} + 2\nu_{dp} = \nu_{lock} \tag{10}$$

where the factor of two is a result of passing through the AOM twice.

Finally, the second AOM allows us to offset the laser frequency such that optical pumping can be achieved,

$$\nu_{op1} = \nu_{laser} + \nu_{AOM} \tag{11}$$

and the RF allows us to split the frequencies for optical pumping such that,

$$\nu_{op2} = \nu_{op1} \pm \nu_{RF} \tag{12}$$

A solution to these equations for our desired frequencies is $\nu_{dp} = 65\, MHz$ and $\nu_{AOM} = 100\, MHz$. In our setup these AOM's are called "AOM 4A" (double pass) and "AOM 12" (single pass) and require $5.508\, V$ and $7.777\, V$, respectively, to obtain the frequency values above.

2.5 Summary and Outlook

A setup was constructed to lock a diode laser to a peak of ^{39}K and then further modified to perform optical pumping. The ability to lock the diode laser was briefly tested and indications were that it is possible to lock to a given peak. However, the stability of the lock was very poor. So, it is important that a reliable method of locking be devised. Upon completion of this, and several other tasks, it will be possible to test the optical pumping in conjunction with the Zeeman magnetic field and see what kind of trapping/polarization is obtained. As of the final writing of this report, flourescence of trapped ^{41}K has been demonstrated with this laser.

References

[1] A. Gorelov, et al., Hyperfine Interactions, **127**, 373, (2000)

[2] D. J. Griffiths, *Introduction to Quantum Mechanics*, Prentice Hall, New Jersey, 1994

[3] D. Halliday, et al., *Fundamentals of Physics, 5th ed.*, John Wiley and Sons, Toronto, 1997

[4] J. D. Jackson, *Classical Electrodynamics, 2nd ed.*, John Wiley and Sons, Toronto, 1975

[5] P. Bennett, Russian Coil Driver Notes, TRIUMF, Vancouver, 1997

[6] Y. C. Chung, "Frequency-Stabilized Lasers and Their Applications", SPIE Proceedings, Vol. 1837, Boston, 1992

[7] C. J. Myatt, N. R. Newbury, and C. E. Wieman, Optics Letters, **18**, 649, (1993)